Dalton Transactions

ROYAL SOCIETY OF CHEMISTRY

PAPER

View Article Online
View Journal | View Issue

Cite this: *Dalton Trans.*, 2026, **55**, 5290

Zn(II) complexation promotes isomerization and oxidative rearrangements of naringenin: evidence from IR ion spectroscopy and DFT calculations

Lucretia Rotari, †[a] Valeria Vergine, †[a] Giel Berden, [b,c] Jos Oomens, [b,c] Barbara Chiavarino, *[a] Davide Corinti *[a] and Maria Elisa Crestoni [a]

Flavonoids are widespread natural polyphenols whose biological activity is closely connected to their ability to coordinate essential transition metals and modulate redox processes. In particular, complexation with metal ions such as Zn(II) can profoundly influence their structural, chemical, and antioxidant properties, with implications for metal trafficking and biological function. In this work, we combine tandem mass spectrometry, infrared multiple photon dissociation (IRMPD) spectroscopy, and density functional theory calculations to elucidate the gas-phase structures and dissociation pathways of Zn(II) complexes with the conjugate base of naringenin (Nar) and its structural chalcone (ChNar) isomer. IRMPD spectra of $[Zn(Nar-H)]^+$ reveal a well-defined coordination motif involving the O4 and O5 oxygen atoms of the flavanone scaffold. Notably, the Zn complex of naringenin chalcone displays an identical spectroscopic fingerprint, suggesting Zn-assisted isomerization of the chalcone into the naringenin form upon metal coordination. When activated, both complexes dissociate to form a fragment at *m*/*z* 271, corresponding to a formally oxidized naringenin species by hydride loss. Spectroscopic characterization of this product suggests a mixture of protonated apigenin and genistein isomers. Mechanistic insight from calculated potential energy surfaces supports this evidence, demonstrating how metal coordination can promote isomerization reactions. Overall, this study highlights the multifaceted role of Zn(II) in directing flavonoid reactivity and redox chemistry and underscores the potential of IRMPD spectroscopy to unravel metal-mediated transformations in bioinorganic systems.

Received 30th December 2025,
Accepted 3rd March 2026

DOI: 10.1039/d5dt03119b

rsc.li/dalton

1. Introduction

Flavonoids are small naturally occurring polyphenols widely present as secondary metabolites in plants, cereals and fruits. They contribute to their color and aroma and are known to protect against (a)biotic stresses and act as UV filters. The increasing recognition of their role in human health includes a broad spectrum of beneficial effects, such as antioxidant action and anti-inflammatory and anticancer properties, which contribute to their notable role in preventing various chronic diseases.

Amply detected in foods and beverages of plant origin, flavonoids comprise a large class of natural phytochemicals occurring as either glycoside derivatives or free aglycones, which include (iso)flavones, flavonols, flavanones and anthocyanidins. Most of them have nutraceutical, pharmaceutical and cosmetic applications. These health-promoting/biological activities are strongly associated with their excellent ability to directly scavenge free radicals[1] and chelate transition metal ions which trigger radical production, thus promoting prevention against atherosclerosis and neurodegenerative diseases.[2–5] New metal-based drugs can thus be developed with enhanced pharmacological potential as compared to native flavonoids.[6] Isomer differentiation of flavonoids is an essential requirement to unveil their metabolism and structure/activity relationships, which relate to modest chemical disparities like the number of hydroxyl groups and their mutual position.

Flavanones constitute a class of flavonoids and represent the first intermediate along their biosynthetic scheme. Flavanones exhibit the characteristic C6–C3–C6 flavan structure, composed of two aromatic rings (A and B) interconnected by a pyranone ring (C), which adopts a flattened chair-like conformation at the C2 and C3 atoms (Fig. 1a).

Naringenin (4′,5,7-trihydroxyflavanone) (Fig. 1b) is a well-known member of this family and stems from stereo-specific isomerization of its structural chalcone isomer (Fig. 1c).

[a]*Dipartimento di Chimica e Tecnologie del Farmaco, Sapienza Università di Roma, Piazzale Aldo Moro 5, 00185 Rome, Italy.*
E-mail: barbara.chiavarino@uniroma1.it, davide.corinti@uniroma1.it
[b]*HFML-FELIX, Toernooiveld 7, 6525ED Nijmegen, The Netherlands*
[c]*Institute for Molecules and Materials, Radboud University, Heyendaalseweg 135, 6525AJ Nijmegen, The Netherlands*
†These authors contributed equally to this work.

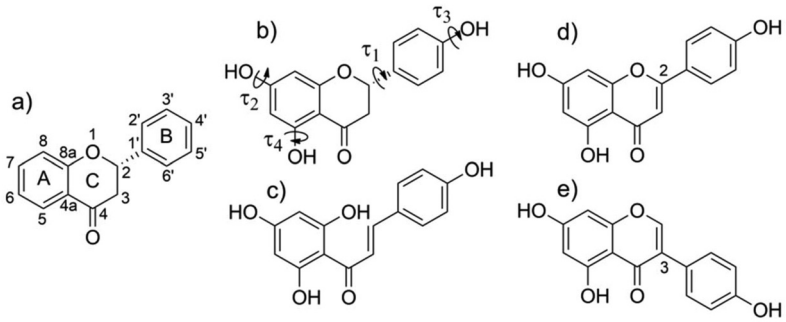

Fig. 1 Schematic representation of (a) the flavanone frame, (b) naringenin, (c) naringenin chalcone, (d) apigenin, and (e) genistein.

Naringenin may undergo further oxidation by dehydration to the flavone apigenin (Fig. 1d) whose antioxidant potential has been evaluated.[7] Naringenin (Nar) is largely present as the (*S*)-enantiomer in the seeds and peels of citrus fruits such as grapefruit and is exploited in perfumery, nutraceutical and medicinal formulations for its flavoring, and hepatoprotective, antibacterial and anticancer effects. Besides, it has been proved as a potential antiviral[8] and cardioprotective[9] agent and as a supplement to be incorporated into specialized functional foods.[10] The three OH substituents at the C5, C7 and C4′ positions play an important role in its radical scavenging and metal chelating properties. Coordination to biologically active metals, like copper, iron and zinc, largely improves the solubility, bioavailability and antiradical ability of Nar, due to the metal's ability to accept and delocalize the electron density of the radical intermediates.[3]

Elucidation of metal–flavonoid binding motifs is relevant to assess how the intricate nature of their interactions may affect metal trafficking and dysregulation, thus orienting potential therapeutic actions.[11,12] Notably, besides the formation of coordination bonds, redox interactions have also been verified, where the donation of electrons from the flavonoid ligand to the transition metal ion may occur irreversibly and reduce metal ions, even to their metallic state.[2,13,14] Interestingly, metal–flavonoid networks have recently been engineered in new hybrid materials as biofunctional films and capsules for applications that range from (nano)medicine to food packaging.[15,16]

A wide scope of experimental techniques, including potentiometric titrations, X-ray crystallography, EPR, NMR and UV-vis spectroscopies, and mass spectrometry (MS),[17,18] have served to assess the physicochemical properties, stability and favorable binding motifs of several flavonoid–metal complexes in the solid state, in solution and in the gas phase.[2,12] Due to its high sensitivity and specificity, MS represents an invaluable technique for flavonoid differentiation, especially in conjunction with liquid chromatography. Among advanced analytical methods to investigate several classes of flavonoids and related *O*- and *C*-glycosides, MS/MS analyses can provide enhanced detection sensitivity and structural information, essentially without sample pretreatment.[19] Enhanced detection sensitivity and improved isomer differentiation of flavonoids, both in the form of aglycones and glycosides, have been obtained by collision-induced dissociation (CID) MS/MS on metal complexes with or without an auxiliary ligand, yielding a larger number of structurally distinct product ions.[20] In particular, coordination of naringenin with Cu(II) and 2,2′-bypridine was found to produce a high signal enhancement.[18] The presence of 1,10-phenanthroline as a co-ligand turned out to be valuable for their cytotoxic activity against malignant cells by an intercalative binding mode.[21] However, unambiguous determination of the molecular structure requires MS to be combined with spectroscopic methods, such as infrared multiple photon dissociation (IRMPD) spectroscopy. This technique relies on a photofragmentation process triggered by the stepwise absorption of multiple resonant IR photons, combined with a fast intramolecular vibrational redistribution (IVR). This process ultimately promotes a wavelength-dependent dissociation typically proceeding along the lowest energy channel.[22] Recording the wavelength-dependent ion abundances by MS allows one to obtain a close representation of the vibrational spectrum of the sampled ionic species.

The present contribution follows up on a previous investigation aimed to directly discriminate the protonated forms of naringenin and its structural isomer, naringenin chalcone. Their geometries were efficiently differentiated by IRMPD spectroscopy, even in samples extracted from natural sources.[23]

This study focuses on the structural characterization of the adducts formed by Zn(II), an essential trace metal, with the conjugate base of Nar and of its structural isomer chalcone (ChNar), in a metal : ligand ratio of 1 : 1, $[Zn(Nar-H)]^+$, $[Zn(ChNar-H)]^+$, respectively, aiming to shed light on their radical scavenging properties and to reveal structural motifs related to biological activity.

The sampled ions, prepared in solution and brought into the gas phase by electrospray ionization (ESI) as bare ions, devoid of any external perturbation, are interrogated by tandem mass spectrometry (MS/MS) and IRMPD spectroscopy, backed by quantum-chemical calculations.[22,24–26] Hitherto, several studies have conveniently exploited IRMPD spectroscopy, shedding light on specific structural and binding features of a variety of (de)protonated and metal-bound (bio)

molecules, including nucleobases,[27] modified amino acids,[28] therapeutics,[29] and metabolites,[30] concurring to discriminate distinct (de)protonation sites and binding schemes.

The present analysis focuses on integrating MS results with spectroscopic features diagnostic of the coordination site in the singly charged adducts, $[Zn(Nar-H)]^+/[Zn(ChNar-H)]^+$, and of any structural clue allied to biochemical activity. Additionally, the nature of the fragmentation product $[Nar-H]^+$ obtained by MS/MS analyses of both metal complexes has been inspected as well by comparison with the computed IR spectra of candidate isomers, including protonated apigenin and genistein (Fig. 1e), and by quantum-chemical investigation of the dissociative redox reaction. The collected evidence expands our understanding of flavanone oxidation and metal reduction and spurs new directions in isomer differentiation.

2. Experimental details

2.1 Materials and MS analysis

All reagents and solvents, including (*S*)-naringenin (CAS number 480-41-1), apigenin (CAS number 520-36-5) and genistein (CAS number 446-72-0), were research-grade products (purity ≥95%) purchased from Merck Life Science S.r.l. (Milan, Italy) and used as supplied. Mass spectrometry experiments were conducted on a linear ion trap mass spectrometer (LTQ XL, Thermo-Fisher Scientific) coupled with an electrospray ionization (ESI) source. The ions of interest are singly protonated apigenin and genistein ($[Api + H]^+$ and $[Geni + H]^+$) and complexes of Zn(II) with naringenin and chalcone ($[Zn(Nar-H)]^+/[Zn(ChNar-H)]^+$), corresponding to the molecular formulas $[C_{15}H_{11}O_5]^+$ at *m*/*z* 271 and $[C_{15}H_{11}ZnO_5]^+$ at *m*/*z* 335–337, respectively. No evidence for doubly charged complexes containing the neutral ligand, *e.g.* $[Zn(Nar)_{1,2}]^{+2}/[Zn(ChNar)_{1,2}]^{+2}$, has emerged. These species were generated by ESI in positive ion mode, ESI(+), by directly infusing a 2 μM apigenin or genistein solution in methanol, and a 5 μM solution of naringenin or chalcone with $ZnSO_4$ (1 : 3 molar ratio); solutions were prepared in water/methanol (1 : 1 v/v) and infused at a flow rate of 150 μl h^{-1}. The $[Nar-H]^+$ ion at *m*/*z* 271 was produced by CID assay of mass-selected $[Zn(Nar-H)]^+/[Zn(ChNar-H)]^+$. CID-$MS^3$ experiments were performed for comparative purposes on primary fragments to map competitive dissociation channels. Usual working parameters were as follows: spray voltage = 5.5 kV, sheath gas (N_2) flow rate = 5 arb. u., sweep gas (N_2) rate = 1 arb. u., capillary voltage = 40 V, tube lens voltage = 80 V and capillary temperature = 275 °C.

2.2 IRMPD spectroscopy

IRMPD spectra of the zinc naringenin complex and protonated apigenin and genistein were recorded at the Free Electron Laser for Infrared eXperiments (FELIX) Facility (Nijmegen, The Netherlands)[31] using a commercial 3D quadrupole ion trap (QIT) mass spectrometer (Bruker AmaZon Speed ETD, Bremen, Germany) modified to allow optical access to trapped ions.[32]

Mass-selected ions were irradiated with a single IR pulse to yield wavelength-dependent infrared multiple photon dissociation. The FEL was operated at a repetition rate of 10 Hz with a pulse energy of 70–100 mJ in the structurally diagnostic "fingerprint" frequency range of 600–1850 cm^{-1}; frequency scans were performed with steps of 5 cm^{-1}. For each step, 6 replicate mass spectra were averaged. To prevent extensive depletion of the parent ions (saturation) and abate the formation of fragment ions beneath the low-mass cut-off of the MS, the spectra were recorded at several levels of laser-pulse energy attenuation.[33]

IR action spectra were collected by recording the photofragmentation yield R ($R = -\ln[I_P/(I_P + \sum I_F)]$), where I_P and I_F are the abundances of the precursor ion and of a photofragment ion, respectively, as a function of photon wavenumber.[34] Also, a linear correction for the frequency-dependent variation in laser pulse energy was applied.[35]

2.3 Computational details

Guess structures of $[Api + H]^+$, $[Geni + H]^+$, $[Nar-H]^+$ and $[Zn(Nar-H)]^+/[Zn(ChNar-H)]^+$ ions were identified by a preliminary conformational survey based on previously described geometries[36,37] and the use of the Conformer Distribution tool as implemented in the Spartan'16 software suite (Wavefunction Inc., Irvine, CA, USA) with the semiempirical PM6 method. In the case of Naringenin, DFT calculations at the B3LYP-D3/6-311++G(d,p) level of theory were performed for *S*-enantiomer geometries, the predominant form in citrus fruits. Several isomers and conformers of the sampled ions were envisioned by exploring different sites of (de)protonation (either hydroxyl groups and saturated C2) and metal binding motifs (either the oxygen atoms of the keto and the phenolic –OH groups), complemented by a systematic stepwise rotation of the torsional angles defined between the two rings AC and B (τ_1, C3–C2–C1′–C2′), and of the three phenolic groups, 5-OH (τ_4, H–O–C5–C6), 7-OH (τ_2, H–O–C7–C8), and 4′-OH (τ_3, H–O–C4′–C3′), as reported in Fig. 1b.[36]

The optimized geometry, thermodynamic properties (electronic energy values, zero point energy (ZPE) and thermal corrections, entropies, and free energies at 298 K) and harmonic vibrational frequencies of the lowest-lying structures were obtained in the gas-phase at the B3LYP-D3/6-311+G(d,p) level of theory, chosen to be consistent with previous reports on structurally similar compounds, such as Cu(II) curcumin.[38] Density functional theory (DFT) calculations were carried out using Gaussian 09 rev.D01.[39] Selected structures were reoptimized at the B2PLYP/Def2TZVP level with vibrational analysis being performed at the same level. The double-hybrid density functional B2PLYP includes an explicit perturbative second-order correlation component in addition to Hartree–Fock exchange and has been shown to improve the accuracy of calculated vibrational properties relative to conventional hybrid functionals.[40,41] Accordingly, B2PLYP results were used for the discussion of the experimental results. Harmonic vibrational frequencies were uniformly scaled by a factor of 0.974 for a better agreement with the IRMPD spectra.[42] Computed

vibrations were also used to verify the stationary points as local minima. For the sake of comparison, the calculated linear IR bands were convoluted by assuming a Gaussian profile with an associated width (fwhm) of 12 cm^{-1}, which accounts for the finite laser bandwidth (0.4% of the IR frequency), unresolved rotational structure of the ions (which are near room temperature), and multiple photon absorption effects.

For the calculation of the dissociation reaction PES, transition states (TS) were identified by the presence of a single imaginary vibrational frequency and were connected to the corresponding reactant and product structures through intrinsic reaction coordinate (IRC) calculations.

3. Results and discussion

3.1 Mass spectra and fragmentation channels

Previous mass spectrometric studies described the formation of naringenin metal complexes with Cu(II), Fe(II) and Fe(III), evidencing different metal : flavanone stoichiometries.[17] Likewise, under the present experiments conditions, ESI(+) direct infusion of a 50 : 50 water/methanol solution of naringenin with $ZnSO_4$ in a 1 : 2 molar ratio produces abundant signals attributed to $[Zn(Nar\text{-}H)]^+$ (*m*/*z* 335). In addition, protonated naringenin, $[Nar + H]^+$(*m*/*z* 273), as well as metal complexes with metal : naringenin ratios of 1 : 2, namely $[Zn(Nar)(Nar{-}H)]^+$ (*m*/*z* 607), and 2 : 3, *i.e.*, $[Zn_2(Nar{-}H)_3]^+$ (*m*/*z* 941) are also observed. Notably, when the chalcone isomer (ChNar) is used as the starting ligand, the same ionic species are observed, indicating comparable reactivity of the two ligands toward Zn^{2+}. As an example, the mass spectrum in Fig. S1 shows the characteristic isotopic patterns of the observed Zn complexes, which reflect the natural abundances of Zn isotopes. In the following, all masses refer to the monoisotopic species of each complex, corresponding to the isotopologue containing ^{64}Zn and ^{12}C. After fine experimental tuning, no doubly charged assemblies like $[Zn(Nar)_{1,2}]^{+2}$/$[Zn(ChNar)_{1,2}]^{+2}$ were observed, in agreement with previous findings, which reported evidence only for metal complexes containing deprotonated flavonoids.[17] Furthermore, the relatively weak abundance of ESI signals was ascribed to a significant formation of electroneutral, MS-undetected adducts, *e.g.* $[Zn(Nar{-}H)_2]^0$, ascribed to the acidity of flavonoid molecules.[18]

The fragmentation behavior of the mass-selected $[Zn(Nar{-}H)]^+$ adduct has been examined by CID experiments, aiming to possibly identify diagnostic products ions. Based on previous reports, a numbering system for free aglycones has been applied in this study for the identification of product ions containing A- and B-rings, specified as $^{ij}A^+$ and $^{ij}B^+$, where the *i* and *j* superscripts specify the broken C–C bonds of the C-ring (Fig. 1).[43] Differently, fragment ions formed by direct loss of radicals or small molecules, including H_2O, CO, C_2H_2O, and C_3O_2, from the precursor ion $[M + H]^+$ are denoted by referencing to it, *e.g.*, $[M + H{-}H_2O]^+$. The CID spectrum of $[Zn(Nar{-}H)]^+$, with monoisotopic mass of the precursor at *m*/*z* 335, displays product ions at *m*/*z* 317 and 307, which imply simple neutral loss of H_2O and CO, respectively (Fig. S2 and Table S1). All of these species retain the zinc atom, as evidenced by the distinct isotope pattern, while two other product ions at *m*/*z* 271 and 243 are due to the elimination of Zn and Zn + CO, respectively. Additional fragmentation channels are observed, the most abundant being those due to loss of C_2H_2O (*m*/*z* 293), Zn + C_2H_2O (*m*/*z* 229), 2CO + $3H_2O$ (*m*/*z* 225), Zn + 3CO (*m*/*z* 187), and Zn + $[C_8H_{10}O]$ (*m*/*z* 149). Notably, the characteristic B ring cleavage arising at *m*/*z* 177 from fragmentation of plain deprotonated naringenin, $[Nar{-}H]^-$,[23] is absent here. At the same time, metal binding in $[Zn(Nar{-}H)]^+$ seems to also stabilize the C-ring and prevent the formation of the $^{1,3}A^+$ ion at *m*/*z* 153 by a retro Diels–Alder (RDA) reaction, which occurs as a prominent fragment from protonated naringenin, $[Nar + H]^+$.[23,44]

About the elimination of ZnCO, other flavonoids were already found to undergo the same cleavage, except for catechins, suggesting the 4-oxo and 5-hydroxyl groups as the metal chelation site.[17]

Almost identical CID spectra are obtained in this study when passing to assay the complexes of the conjugate base of chalcone with Zn (Fig. S2). Former evidence on $[Nar + H]^+$ and $[ChNar + H]^+$ showed that, while CID hardly distinguished these isomers, IRMPD spectroscopy succeeded in their discrimination.[23] Herein, we accordingly decided to probe the structure of $[Zn(Nar{-}H)]^+$/$[Zn(ChNar{-}H)]^+$ by IR ion spectroscopy, as will be described in the next section.

3.2 Structural and vibrational analysis of naringenin and naringenin chalcone complexes with zinc(II)

The vibrational features of the zinc complexes $[Zn(Nar\text{-}H)]^+$ and $[Zn(ChNar\text{-}H)]^+$ have been recorded as mass-isolated ions inside the mass spectrometer, *i.e.* free of any external perturbation, in the mid-IR domain (600–1800 cm^{-1}), which comprises highly structurally informative modes.[45] Structural evidence on the interaction of naringenin with another dication, Cu(II), was obtained in the crystalline and solution phases,[3,12,21] revealing the dominance of metal coordination through the oxygens of the C4-keto (C ring) and adjacent deprotonated C5-hydroxy (A ring) donors, in a keto-phenoxide structure. Metal chelation turned out to alter the electronic distribution and enhance the antiradical property of deprotonated naringenin. The experimental spectrum recorded for $[Zn(Nar\text{-}H)]^+$ exhibits numerous pronounced absorptions, including an intense peak at 1608 cm^{-1}, a broad band (FWHM = 60 cm^{-1}) centered at 1482 cm^{-1}, along with a band at 1405 cm^{-1}. Below 1300 cm^{-1}, a partly resolved peak at 1262 cm^{-1} is followed by the most intense band of the spectrum at 1168 cm^{-1} with a shoulder at 1206 cm^{-1}. Weaker features are recorded at 1085, 830 and 715 cm^{-1} (Fig. 2). Interestingly, $[Zn(ChNar\text{-}H)]^+$ (Fig. S3) exhibits the same vibrational profile, suggesting the chalcone to flavone isomerization process to be favored by the binding with the metal.

To aid in the interpretation of the observed spectra, an extensive exploration has been performed to identify the minimum energy structures of $[Zn(Nar{-}H)]^+$ by DFT calcu-

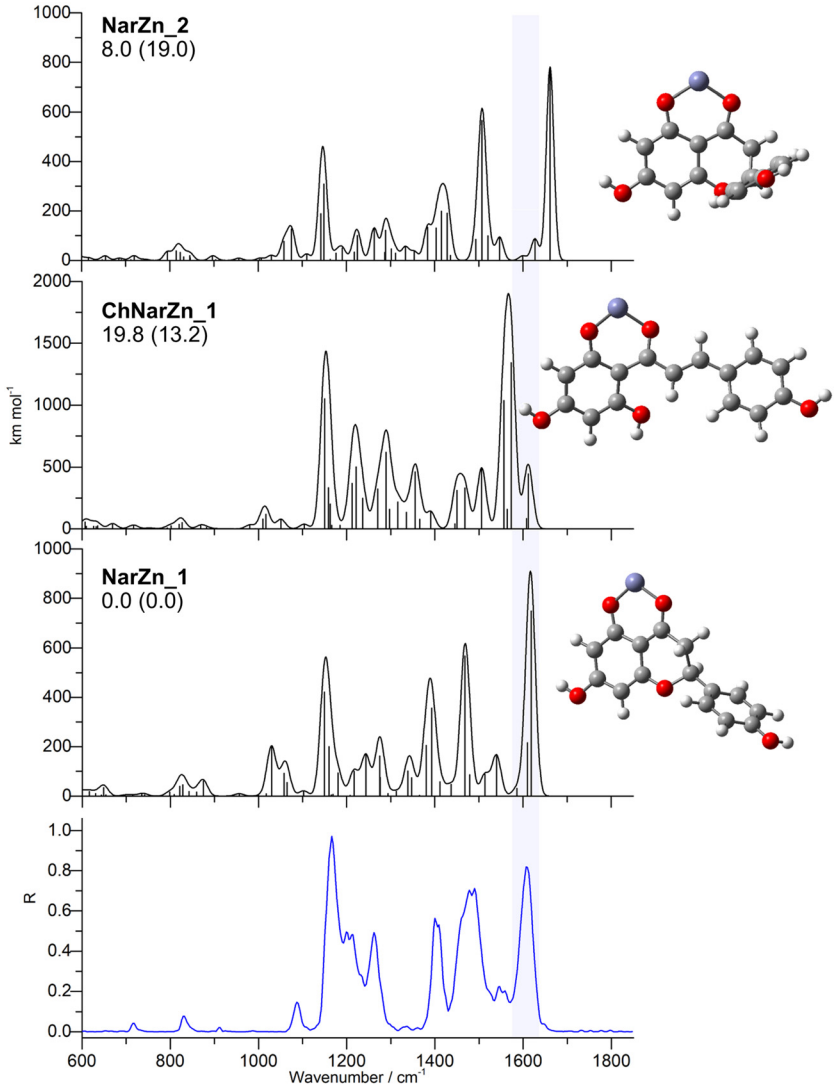

Fig. 2 IRMPD spectrum of $[Zn(Nar-H)]^+$ compared to the calculated IR spectra of **NarZn_1**, **ChNarZn_1** and **NarZn_2** at the B2PLYP level with their optimized geometries. Relative enthalpies (free energies) at 298 K are reported in kJ mol^{-1}.

lations at the B3LYP/6-311++G(d,p) level, which are reported in Fig. S4, along with relative energies and the calculated IR spectra. The optimized geometries consider several potential binding motifs for Zn, with the metal interacting with the O-atoms of the keto-phenoxide group, or either of the phenate sites, *i.e.*, 7-OH or 4′-OH, as well as with the deprotonated C3 methylene group. As previously described, naringenin's phenol ring may adopt two arrangements with respect to the pyranone chair-like, either in the equatorial (**C2** form) or the axial (**C1** form) position. Besides, 7-OH and 4′-OH may bear two opposite orientations with torsional angles (∠HOC4′C3′ and ∠HOC7C8) of either 0 (anticlockwise) or 180 (clockwise) degrees.[46] The relevant thermodynamic data, including the relative enthalpy (ΔH°_{rel}) and free energy (ΔG°_{rel}) values at 298 K (kJ mol^{-1}), are presented in Table S2.

The optimized global minimum (GM) conformer **NarZn_1** exhibits the zinc ion bound to the keto-phenoxide site (4-C═O/5-OH), thus forming a rigid six-membered ring, where the metal–oxygen distances are 1.806 and 1.841 Å, the B ring is in the equatorial position, the ∠C2′C1′C2C3 dihedral angle $\tau 1$ is equal to 62.1° and the hydroxyl groups are coplanar with the aromatic rings (Fig. 2).

When the C1 → C2 interconversion occurs by rotation around the C2C3 bond, a decrease in relative stability of 19.1 kJ mol^{-1} at the B2PLYP level is observed, thus leading to **NarZn_2** rotamer with the dihedral angle $\tau 1$ equal to −55.4°. This process has been stated to entail a small free energy barrier for bare neutral naringenin (15.7 kJ mol^{-1}) and a little influence on structural setting.[46] Another keto-phenoxide zinc complex has been examined, **ChNarZn_1**, lying 13.2 kJ mol^{-1} higher in energy at the B2PLYP level. It is characterized by an open, slightly tilted chalcone-like structure, with a double bond Cα═Cβ, and a clockwise arrangement of hydroxyl groups.

Different deprotonation sites can engage in zinc binding, either the 7-OH phenol group or the methylene $C3H_2$ site, but lead to less favorable isomers, such as **NarZn_5** and **NarZn_3**, placed at 131.1 and 79.9 kJ mol^{-1} of relative energy at the B3LYP level, respectively. Although these geometries benefit from an equatorial arrangement (**C2**) and a strong intramolecular H bond between 5-OH and the adjacent C4═O carbonyl site ($r_{5OH\cdots O=C}$ = 1.869 and 1.737 Å for **NarZn_3** and **NarZn_5**, respectively), it turns out that the lack of C4═O/5-OH in zinc coordination produces a major destabilization in both structures. Metalation at the deprotonated 4′-OH has been also explored, generating a structure at a relative energy of 107.1 kJ mol^{-1} at the B3LYP level (**NarZn_4**).

From the comparative examination of Fig. 2, frequencies and (partially) intensities of the main experimental bands of $[Zn(Nar-H)]^+$ are well interpreted by the calculated IR modes of the lowest energy structure **NarZn_1**. Vibrational frequency analysis of the global minimum **NarZn_1** allows the assignment of the major IRMPD absorptions, as summarized in Table S3 together with a brief mode description. The most intense experimental band, observed at 1168 cm^{-1}, may be attributed to the in-plane O4′–H bending coupled with C–H bending motions, in line with the computed mode at 1164 cm^{-1}. The broad prominent feature at 1608 cm^{-1} may correspond to the CO stretching vibrations of the C4′ and C7 phenol groups coupled to the CC stretching motions of the corresponding rings calculated at 1617 and 1625 cm^{-1}, respectively, supporting coordination of the metal ion at the C5 and C4 carbonyl oxygens. A weak band at 1549 cm^{-1} can be assigned to a combination of C–C–C asymmetric stretching and O7–H bending, while the intense signal at 1482 cm^{-1} is likely attributable to the coupled C4–O and C5–O stretching modes computed at 1474 cm^{-1}, reflecting the perturbation of the C–O bonds upon Zn binding. The high-intensity band at 1405 cm^{-1} is finally in agreement with C3–H_2 scissoring and C4–O stretching motions.

In the 1300–1200 cm^{-1} region, the band at 1262 cm^{-1} can be attributed to C4′–O4′ stretching and ring B C–H bending and the shoulder at 1206 cm^{-1} may involve O7–H bending and C3–H_2 twisting. The dominant 1168 cm^{-1} absorption is followed by weaker features, including a small band at 1085 cm^{-1}, which may correspond to C–C and C4a–C8a stretching, and a minor band at 830 cm^{-1} possibly due to C2–O1 stretching. Finally, the very weak signal at 715 cm^{-1}, reproduced by the calculated mode at 670 cm^{-1}, can be assigned to a O–Zn–O asymmetric stretching coupled with ring A breathing.

The **NarZn_2** rotamer shares similar absorptions and its presence in the sampled ion population cannot be ruled out. However, the calculated vibrational mode of the C7–O stretching is blue-shifted to 1660 cm^{-1} compared to the corresponding mode of **NarZn_1**, suggesting that **NarZn_2** contributes only marginally to the ion population, given that the experimental IR band appears at 1608 cm^{-1}. In contrast, the IR spectrum of **ChNarZn_1** calculated at the B2PLYP level, although matching several experimental features, predicts a strong absorption at 1355 cm^{-1} which corresponds to a convoluted vibrational mode involving the stretching of CC bonds across the entire ion and the in-plane bending of the three free OHs. Such an intense feature is not seen experimentally; instead, the very weak band at 1334 cm^{-1} better matches the in-plane O4′–H and C–H bending vibrations predicted for **NarZn_1**. At the same time, the relatively high intensity of the shoulder at 1206 cm^{-1} on the band at 1168 cm^{-1} may indicate a minor contribution from **ChNarZn_1**, which shows convoluted CH bending vibrational modes calculated at 1221 and 1207 cm^{-1}. Such evidence suggests that the open isomer may partially contribute to the gas-phase population. Interestingly, given that the IRMPD spectrum of $[Zn(ChNar-H)]^+$ is superimposable to that of $[Zn(Nar-H)]^+$, it is reasonable to assume that both species belong to the same gas-phase population, predominantly composed of **NarZn_1** with a minor contribution from **ChNarZn_1**. This, in turn, suggests that the interaction with the Zn(II) ion may promote the isomerization reaction, leading preferentially to the closed form, which is also energetically favored in its interaction with zinc. In fact, no isomerization reactions were observed for the protonated ions $[Nar + H]^+$ and $[ChNar + H]^+$, which showed distinct IRMPD spectra.[23] Finally, **NarZn_5**, **NarZn_3**, and **NarZn_4** are probably not populated based on both spectroscopic and theoretical evidence. Indeed, their IR spectra calculated at the B3LYP level (Fig. S4) show bands associated with the C4–O stretching mode, which is not coordinated to zinc, appearing above 1600 cm^{-1}, a region where the experimental spectrum is silent. Overall, these results indicate **NarZn_1** as the most probable geometry of bare $[Zn(Nar-H)]^+$, with possible contributions of the low-lying **NarZn_2** conformer. Both structures are stabilized by a six-membered ring, where the carbonyl and 5-OH oxygen atoms of deprotonated naringenin are engaged in Zn(II) chelation. Contributions from higher-energy isomers can be spectroscopically excluded, while a limited participation of the open-form **ChNarZn_1** is supported by spectroscopic evidence, highlighting the role of metal ions in promoting naringenin–chalcone isomerization.

3.3 Structural and vibrational analysis of fragment ions $[Nar-H]^+$

Interestingly, the fragment ion at *m*/*z* 271 obtained by both CID and IRMPD of $[Zn(Nar-H)]^+$ has previously been attributed to $[Nar-H]^+$, formed through a process involving the reduction of the metal ion at the expense of flavanone oxidation through a formal hydride loss.[17] Although the present metal complexes represent highly simplified models of the real system, the redox pathway identified in this study may suggest that a similar mechanism underlies the protective role of flavonoids against copper-induced low-density lipoprotein (LDL) oxidation in atherosclerotic lesions. To obtain structural information on this fragment ion, CID-MS^3 experiments on *m*/*z* 271 produced by dissociation of $[Zn(Nar-H)]^+$ were compared with the CID-MS^2 spectra of potential isobaric candidates, specifically the protonated form of apigenin and genistein, $[Api + H]^+$ and $[Geni + H]^+$, respectively (Fig. S5). In agree-

ment with previous studies describing rearrangement and fragmentation processes of (de)protonated flavonoids by tandem MS,[47,48] the three ions investigated here at *m/z* 271 generate common fragments at *m/z* 145 ($^{0,4}B^+$-H_2O), 153 ($^{1,3}A^+$), 225 (H_2O + CO loss), and 243 (CO loss); however, characteristic product ions are also observed. In particular, *m/z* 203 (C_3O_2 loss) and 229 (C_2H_2O loss) are specific of $[Api + H]^+$, whereas $[Geni + H]^+$ produces distinct fragments at *m/z* 253 (H_2O elimination), *m/z* 215 and 187, by release of two and three molecules of CO, respectively, as well as *m/z* 149, by CO and B-ring loss. Notably, the fragmentation pattern of the oxidized form of naringenin produced upon activation of the metal complex, formally denoted as $[Nar–H]^+$ (*m/z* 271), includes not only product ions characteristic of $[Api + H]^+$, previously identified as the result of dehydrogenation of naringenin, but also those typical of $[Geni + H]^+$. Consequently, unequivocal structural assignment of $[Nar–H]^+$ based solely on fragmentation patterns remains challenging. To address this limitation, IRMPD spectroscopy was employed to elucidate the vibrational signatures and structures of the *m/z* 271 ions $[Api + H]^+$ and $[Geni + H]^+$. The spectroscopic features of the fragment ions at *m/z* 271, $[Nar–H]^+$, generated by CID of $[Zn(Nar–H)]^+$ have been also analyzed in the same spectral range and compared with the IRMPD spectra of *m/z* 271 formed by protonation of native apigenin and genistein. The resulting IRMPD spectra are displayed in Fig. 3.

The IRMPD spectra of $[Api + H]^+$ and $[Geni + H]^+$, reported and discussed for the first time here, serve as a reference for structural assignment of the $[Nar–H]^+$ fragment. The two isomers differ only in the position of the phenolic group (C2 in apigenin; C3 in genistein). As expected in consideration of this modest structural change, their IR spectra are largely similar. The most notable differences include: (1) an intense band at ~1290 cm^{-1}, significantly stronger in $[Geni + H]^+$; (2) a cluster of absorptions from 1500 to 1700 cm^{-1}, where $[Geni + H]^+$ displays a dominant feature blue-shifted by ~25 cm^{-1} relative to $[Api + H]^+$ (Tables S4 and S5). Intriguingly, the IRMPD spectrum of the *m/z* 271 ion derived from $[Zn(Nar–H)]^+$ exhibits vibrational features consistent with a mixed population of both isomers, strongly suggesting a 1,2-shift of the phenolic group, from C2 in naringenin to C3 in the genistein structure, during metal-mediated oxidation. Specifically, the highest-frequency band at 1598 cm^{-1} (highlighted in pale green in Fig. 2) is closer to the absorption observed for $[Api + H]^+$; however, its broader profile suggests contributions from additional bands, such as those of $[Geni + H]^+$ at 1614 and 1588 cm^{-1}. Further evidence for the presence of $[Geni + H]^+$ in the gas-phase population is provided by the band at 1504 cm^{-1} (highlighted in red). Contributions from both $[Api + H]^+$ and $[Geni + H]^+$ are further supported by the spectroscopic activity of $[Nar–H]^+$ below 1400 cm^{-1}, where three weaker absorptions are observed. In particular, the feature around 1300 cm^{-1} (highlighted in red) is consistent with the spectrum of $[Geni + H]^+$, while the most intense band of the spectrum at 1156 cm^{-1} (highlighted in green) better matches the characteristic absorption of $[Api + H]^+$.

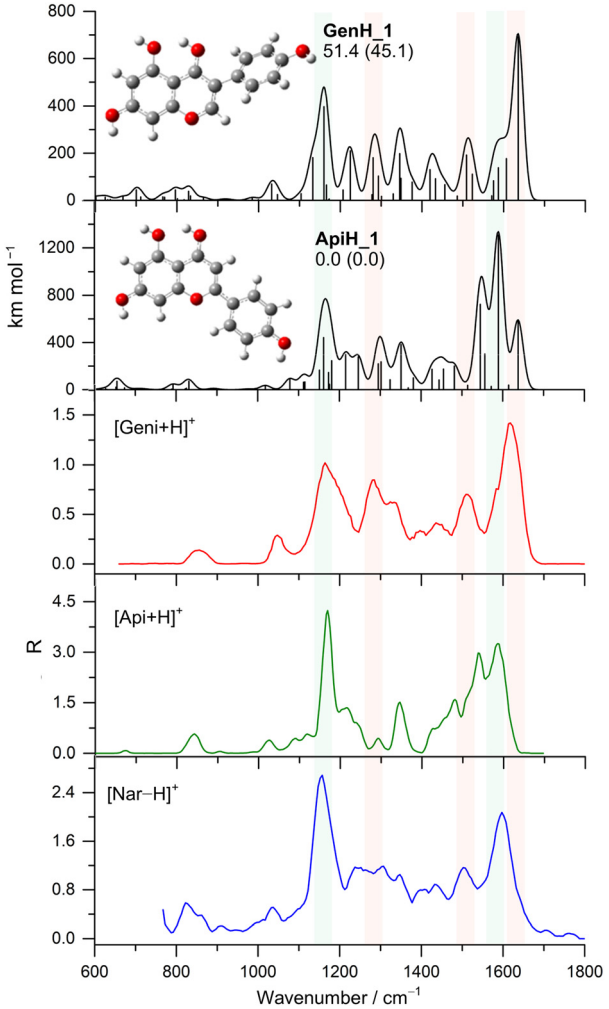

Fig. 3 IRMPD spectrum of $[Geni + H]^+$, $[Api + H]^+$ and $[Nar–H]^+$, red, green and blue profiles, respectively, compared to the calculated IR spectra of the lowest energy conformers of protonated apigenin (**ApiH_1**) and genistein (**GenH_1**) at the B2PLYP level with their optimized geometries. Relative enthalpies (free energies) at 298 K are reported in kJ mol^{-1}.

Both the $[Api + H]^+$ and $[Geni + H]^+$ IRMPD spectra were compared with the calculated IR spectra of a series of possible conformers and isomers of the two species for the assignment of the vibrational modes and, ultimately, to structurally characterize the assayed gas-phase ions. All the calculated spectra and corresponding geometries with relative free energies at 298 K are reported in Fig. S6–S10. Regarding $[Api + H]^+$, different conceivable protonation sites were explored, specifically the O4 atom and the C2 and C3 atoms (Fig. S6–S8). Among them, protonation at O4 is strongly energetically favored. Accordingly, the subsequent exploration of the conformational space, performed by rotating the hydroxyl groups at C4, C5, C7 and C4′, is based solely on the protomer protonated at O4. Among the different structures obtained, the **ApiH_1** isomer corresponds to the global minimum and shows the O4H and O5H hydroxyl groups oriented in the opposite direc-

tion of the phenol group. This is the most important structural aspect energetically; in fact, rotation by 180° of both OH groups, while keeping the hydrogen bond between them intact, increases the energy by 17.1 kJ mol^{-1}. Turning the OH groups at C4′ and C7, on the other hand, generates almost degenerate conformers (**ApiH_2-4**).

The same discussion applies to [Geni + H]$^+$; indeed, the global minimum **GenH_1** shows the same configuration of the C4, C5, C7 and C4′ OH groups of **ApiH_1**. In the case of [Geni + H]$^+$, however, rotation of the OH groups at C4 and C5 does not impact the energy as much as in [Api + H]$^+$; the conformer **GenH_3** is only 1.1 kJ mol^{-1} higher in energy (Fig. S10). Based on the comparison between the calculated spectra of the different isomers and the experimental data, and taking into account the relative thermodynamic stabilities, the conformers **ApiH_1-4** and **GenH_1,2,7** and **8**, differing only by rotations of the OH groups at the C4′ and C7 positions, can be assigned to the gas-phase population of the two ions, respectively. In contrast, the presence of isomers involving rotations of the OH groups at C4 and C5 can be spectroscopically excluded, as these structures exhibit calculated vibrational modes above 1650 cm^{-1}, a spectral region where no experimental absorption is observed (Fig. S8 and S10). For simplicity, only the global minima **ApiH_1** and **GenH_1** will be discussed in detail. For this purpose, these structures were reoptimized at the B2PLYP/def2-TZVP level, and their structures, vibrational features and energies (referring to the lowest-energy one among the two, **ApiH_1**) are reported in Fig. 3. The vibrational assignments are tabulated in Tables S4 and S5, and in the subsequent section a brief description of the experimental bands as a function of the calculated vibrational modes of the lowest-energy isomer is provided.

The fingerprint region of the protonated apigenin IRMPD spectrum is dominated by strong aromatic and C–O related skeletal vibrations. The intense band(s) near 1589 cm^{-1} may be assigned to C–C stretches of rings A/C coupled with in-plane C–H bending motions; a related feature at 1545–1537 cm^{-1} can be attributed to additional C–C stretches with contributions from C4/C7 O–H in-plane bending. The absorption at 1480–1455 cm^{-1} likely arises from mixed C–C stretching and in-plane C–H bending, including contributions from ring B. Features in the 1430–1427 cm^{-1} region can be interpreted as C–C/C–O skeletal motions (C–C and C4–O stretches) and in-plane C–H bending. In the 1350–1300 cm^{-1} region, the modes near 1351–1324 cm^{-1} may correspond to in-plane H bending motions of ring B and in-plane O–H bending (C4, C5), often mixed with C–C stretching contributions. Bands around 1294–1240 cm^{-1} appear to involve C4′–OH/C5–OH stretching and associated β H motions of ring B and adjacent carbons. The region 1216–1151 cm^{-1} shows multiple moderate to strong absorptions that can be assigned to the combinations of C–O (C4–OH, C5–OH), C–H in-plane bending and ring skeletal motions; notably, bands near 1161–1151 cm^{-1} are consistent with the in-plane H-bending of the aromatic rings and O–H in-plane bending. Lower-frequency features, including the band at 1025–1079 cm^{-1}, may reflect C5–OH stretching together with ring breathing modes, while weak absorptions at ~844 cm^{-1} and ~677 cm^{-1} are characteristic of out-of-plane C–H and O–H deformations, respectively. Moving to [Geni + H]$^+$, the strong absorption at 1614 cm^{-1} may be assigned to the C–C stretching of ring A, while bands in the 1588–1575 cm^{-1} range likely reflect additional aromatic C–C stretches, some coupled with H-bending motions. The 1514–1509 cm^{-1} region can be interpreted as mixed C–C stretching and in-plane O–H bending (C4 and C7) contributions, and the cluster of bands around 1440–1419 cm^{-1} appears to involve C–O (C5–OH, C4–OH) stretches together with aromatic C–C and C–H in-plane deformations. A pronounced feature at 1329–1293 cm^{-1} may be assigned to in-plane O–H bending (C4, C5) combined with ring skeletal motion. The 1225–1190 cm^{-1} bands can be related to C5–OH/C4′–OH stretching and CH in-plane motions, whereas the very intense absorption at 1164–1133 cm^{-1} is consistent with strong in-plane O–H and C–H bending motions (notably the O4′ in-plane bend and adjacent ring H vibrations). The 1045–1032 cm^{-1} feature is indicative of C5–OH stretching coupled to ring A/C breathing, while low-frequency out-of-plane C–H and O–H deformations appear at 856 cm^{-1} and 701 cm^{-1}.

3.4 PES for the dissociation reaction of [Zn(Nar-H)]$^+$

Experimental spectroscopic data have demonstrated that the fragment at *m*/*z* 271, generated by dissociation of [Zn(Nar−H)]$^+$, constitutes a mixture of protonated genistein and apigenin. This observation opens interesting scenarios in the oxidative evolution of the metabolite naringenin in the presence of Zn^{2+}, which effectively acts as an activator for a 1,2-shift of the phenol ring. This surprising behavior is evaluated here from a thermochemical point of view by employing calculated potential energy surfaces for the two competitive pathways that lead to protonated apigenin and genistein (Fig. 4).

The first step of the proposed dissociation mechanism is a hydride transfer from C3 to O4, occurring upon conversion of **NarZn_1** into **Int1**. The activation energy for this process is high, amounting to 283.6 kJ mol^{-1}. This evidence agrees with the fact that this fragmentation channel is not the first to appear, but competes with water loss and C_2H_2O loss, as evidenced from the CID spectrum shown in Fig. S2. Once the hydride transfer has occurred, the Zn atom moves farther away from O4. Subsequently, both the O5–Zn interaction and the O4H hydroxyl group can rotate with a barrier (**TS2** at 181.2 kJ mol^{-1}) that is significantly lower than the entrance activation energy (**TS1**), leading to **Int2** (140.6 kJ mol^{-1}). Following the initial hydride transfer, the Zn–ligand interaction is significantly weakened, as evidenced by the displacement of the metal center away from the O4 site. Despite extensive exploration, no stable Zn-bound intermediates or transition states connecting **Int2** to the subsequent rearrangement pathways could be located. Therefore, we propose that Zn-loss occurs at this stage, yielding **Int2***, an intermediate structure with no imaginary frequencies observed and a relative free energy of 202.1 kJ mol^{-1}. Although **Int2*** corresponds to a genuine local

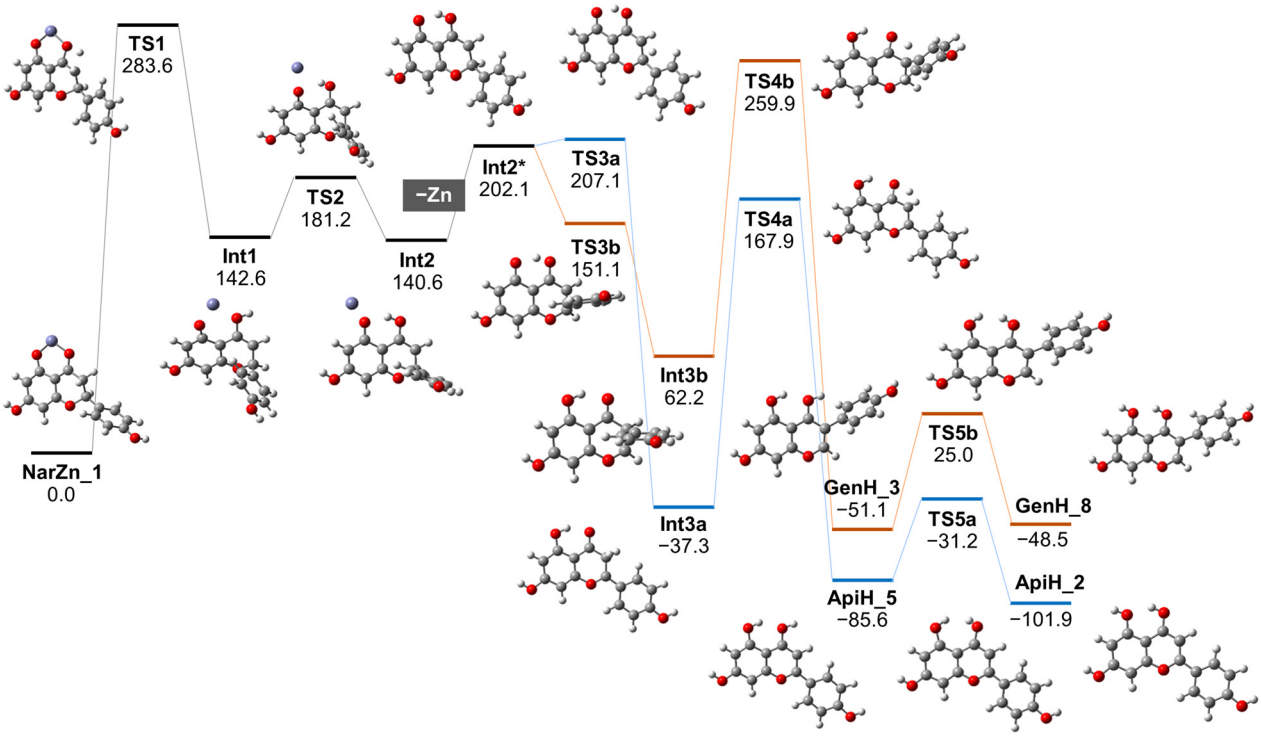

Fig. 4 PES for the dissociation reaction of **NarZn_1** leading to **GenH_8** and **ApiH_2**. Gibbs energies at 298 K at the B3LYP/6-311++G(d,p) level are reported in kJ mol^{-1} together with the structure name. All energies are relative to the Gibbs energy of the reactants. Optimized structures are reported.

minimum on the potential energy surface, it is reached after dissociation of the Zn atom, a high-energy process that leaves the system dynamically activated. Consequently, subsequent rearrangements may proceed downhill on the potential energy surface *via* submerged transition states.[49] From this point onward, two reaction pathways can be envisaged.

- The first pathway, leading to protonated apigenin, is labeled with "a" and reported in blue in the PES (Fig. 4). The initial step is barely higher in energy than **Int2***: **TS3a** lies in fact at 207.1 kJ mol^{-1} and corresponds to a hydride transfer from C2 to C3. The resulting structure **Int3a** is even lower in free energy than the starting complex, being calculated at −37.3 kJ mol^{-1}. The subsequent step is a proton transfer, from C3 to O4, with an activation energy of 167.9 kJ mol^{-1}, leading to **ApiH_5**. In this geometry apigenin is protonated at O4, and the two hydroxyl groups at C4 and C5 are oriented toward the C ring, thus adopting a relatively high-energy conformation. Finally, rotation of both hydroxyl groups can occur with an activation energy of 54.4 kJ mol^{-1}, yielding **ApiH_2**, a rotamer of the global minimum of protonated apigenin, lying only 0.8 kJ mol^{-1} higher in free energy (Fig. S7).

- The second pathway, shown in orange in Fig. 4, leads to the formation of protonated genistein. Interestingly, the first step of this reaction is barrierless: **TS3b**, corresponding to the shift of the phenol ring from C2 to C3, lies at 151.1 kJ mol^{-1}, that is, lower than the transition state proposed for apigenin formation. The resulting intermediate, **Int3b**, is nevertheless higher in energy than **Int3a**, indicating that the phenol-ring shift, while kinetically favored relative to hydride transfer, is thermodynamically less favorable. As in pathway a, a subsequent proton transfer from C3 to O4 occurs. In this case, the associated activation energy is 259.9 kJ mol^{-1}, higher than that of the corresponding step in pathway a (**TS4a** at 167.9 kJ mol^{-1}), but still lower than the initial activation barrier and therefore accessible during the dissociation process. Also along this pathway, rotation of both hydroxyl groups is expected to require only a limited amount of energy; however, the two resulting structures, **GenH_3** and **GenH_8** (also a rotamer of **GenH_1** as shown in Fig. S9), are nearly degenerate in free energy, and no clear preference for either structure can be identified.

4. Conclusions

In this work, IRMPD spectroscopy and quantum-chemical calculations have been combined to investigate the gas-phase structure, reactivity and dissociation behavior of Zn(II)-complexed naringenin. The IRMPD spectrum of $[Zn(Nar–H)]^+$ unambiguously indicates a coordination motif where the Zn center interacts with the O4 and O5 oxygen atoms of the flavonoid scaffold. Remarkably, the IRMPD spectrum obtained for the Zn complex of naringenin chalcone is indistinguishable from that of $[Zn(Nar–H)]^+$, providing direct spectroscopic evi-

dence that the chalcone isomer undergoes Zn-assisted cyclization to the naringenin form upon complexation. However, whether this process occurs in the solution phase or during the ESI process remains unclear.

Upon either collisional or infrared multiple-photon activation, both CID and IRMPD experiments reveal a dominant dissociation channel leading to a fragment at *m*/*z* 271, corresponding to a formally oxidized form of naringenin by hydride loss. IRMPD spectroscopy of this fragment, in combination with reference spectra, demonstrates that it cannot be assigned to a unique flavonoid structure. Instead, the experimental data are consistent with a mixture of two isomeric species, *i.e.*, protonated genistein and apigenin.

The mechanistic origin of this unexpected product distribution has been rationalized through the exploration of calculated potential energy surfaces. These calculations reveal that Zn plays an active role in promoting skeletal rearrangements of the flavonoid core, enabling 1,2-shifts of the phenol moiety. In this way, activation of the Zn complex leads to the formation of both protonated apigenin and genistein. The calculated energetics further explain the simultaneous observation of both species under IRMPD conditions, with apigenin being thermodynamically favored and genistein kinetically accessible.

Overall, this study highlights the ability of metal complexation to profoundly alter the gas-phase chemistry of polyphenolic metabolites, inducing structural rearrangements and isomerization processes. These findings provide new insight into Zn-mediated activation pathways of flavonoids and underscore the power of combining action spectroscopy with theoretical modeling to unravel complex dissociation mechanisms in metal-containing systems.

Author contributions

Lucretia Rotari: investigation; formal analysis; visualization; writing – original draft. Valeria Vergine: investigation; formal analysis; data curation; writing – review & editing. Giel Berden: investigation; resources; methodology; infrastructure support. Jos Oomens: resources; infrastructure support; writing – review & editing. Barbara Chiavarino: investigation; writing – original draft; supervision; funding acquisition. Davide Corinti: conceptualization; investigation; writing – original draft; supervision; funding acquisition. Maria Elisa Crestoni: validation; project administration; supervision; writing – review & editing.

Conflicts of interest

The authors declare no competing financial interest.

Data availability

The data supporting this article are included in the supplementary information (SI). Supplementary information: figures presenting mass spectra and fragmentation spectra of the species of interest; calculated IR spectra at the B3LYP level for isomers and conformers of $[Zn(Nar\text{-}H)]^+$, as well as for protonated genistein and apigenin; and tables reporting thermodynamic data and assignments of vibrational modes. See DOI: https://doi.org/10.1039/d5dt03119b.

Acknowledgements

This work was supported by the Università di Roma La Sapienza-Progetti Medi 2024, grant number RM12419107EFD7BD, from LASERLAB-EUROPE (grant agreement no. 871124, European Union's Horizon 2020 Research and Innovation Programme) and by PE00000003 (decree 776 1550, 11.10.2022) ("ON Foods – Research and innovation network on food and nutrition Sustainability, Safety and Security – Working ON Foods") from the Italian Ministry of University and Research (Sapienza University CUP B53C22004030001) under the National Recovery and Resilience Plan (NRRP), funded by the European Union – NextGenerationEU. We gratefully acknowledge the Nederlandse Organisatie voor Wetenschappelijk Onderzoek (NWO) for the support of the FELIX Laboratory.

References

1 M. Cavia-Saiz, M. D. Busto, M. C. Pilar-Izquierdo, N. Ortega, M. Pérez-Mateos and P. Muñiz, *J. Sci. Food Agric.*, 2010, **90**, 1238–1244.
2 A. Kola, D. Dudek and D. Valensin, *Curr. Med. Chem.*, 2021, **28**, 7278–7294.
3 G. Celiz, S. A. Suárez, A. Arias, J. Molina, C. D. Brondino and F. Doctorovich, *BioMetals*, 2019, **32**, 595–610.
4 R. A. Dixon and G. M. Pasinetti, *Plant Physiol.*, 2010, **154**, 453–457.
5 S. Singh, A. Sharma, V. Monga and R. Bhatia, *Crit. Rev. Food Sci. Nutr.*, 2023, **63**, 8868–8899.
6 E. Halevas, B. Mavroidi, G. Zahariou, M. Pelecanou and A. G. Hatzidimitriou, *Inorg. Chim. Acta*, 2023, **546**, 121325.
7 R. Cai, X. Li, B. Chen, Y. Xie, H. Xie and D. Chen, *ChemistrySelect*, 2019, **4**, 5155–5159.
8 N. Clementi, C. Scagnolari, A. D'Amore, F. Palombi, E. Criscuolo, F. Frasca, A. Pierangeli, N. Mancini, G. Antonelli, M. Clementi, A. Carpaneto and A. Filippini, *Pharmacol. Res.*, 2021, **163**, 105255.
9 E. O. Ilkay, F. N. Seyed, D. Maria, C. T. Gian, M. Kowsar and M. N. Seyed, *Curr. Pharm. Biotechnol.*, 2015, **16**, 245–251.
10 J. Mayneris-Perxachs, J. M. Alcaide-Hidalgo, E. de la Hera, J. M. del Bas, L. Arola and A. Caimari, *J. Funct. Foods*, 2019, **61**, 103504.
11 V. J. Lee and M. C. Heffern, *Front. Chem.*, 2022, **10**, 972198.
12 P. K. Walencik, R. Choińska, E. Gołębiewska and M. Kalinowska, *Molecules*, 2024, **29**, 2573.

13 A. Kola, F. Nencioni and D. Valensin, *Molecules*, 2023, **28**, 5467.
14 N. R. Perron and J. L. Brumaghim, *Cell Biochem. Biophys.*, 2009, **53**, 75–100.
15 N. Bertleff-Zieschang, M. A. Rahim, Y. Ju, J. A. Braunger, T. Suma, Y. Dai, S. Pan, F. Cavalieri and F. Caruso, *Chem. Commun.*, 2017, **53**, 1068–1071.
16 M. A. Rahim, S. L. Kristufek, S. Pan, J. J. Richardson and F. Caruso, *Angew. Chem., Int. Ed.*, 2019, **58**, 1904–1927.
17 M. T. Fernández, M. L. Mira, M. H. Florêncio and K. R. Jennings, *J. Inorg. Biochem.*, 2002, **92**, 105–111.
18 M. Satterfield and J. S. Brodbelt, *Anal. Chem.*, 2000, **72**, 5898–5906.
19 M. S. Sammani, S. Clavijo and V. Cerdà, *TrAC, Trends Anal. Chem.*, 2021, **138**, 116220.
20 J. Zhang, J. Wang and J. S. Brodbelt, *J. Mass Spectrom.*, 2005, **40**, 350–363.
21 L. V. Tamayo, L. R. Gouvêa, A. C. Sousa, R. M. Albuquerque, S. F. Teixeira, R. A. de Azevedo, S. R. W. Louro, A. K. Ferreira and H. Beraldo, *BioMetals*, 2016, **29**, 39–52.
22 J. Oomens, B. G. Sartakov, G. Meijer and G. von Helden, *Int. J. Mass Spectrom.*, 2006, **254**, 1–19.
23 D. Corinti, L. Rotari, M. E. Crestoni, S. Fornarini, J. Oomens, G. Berden, A. Tintaru and B. Chiavarino, *J. Agric. Food Chem.*, 2023, **71**, 4005–4015.
24 T. D. Fridgen, *Mass Spectrom. Rev.*, 2009, **28**, 586–607.
25 J. Roithová, *Chem. Soc. Rev.*, 2012, **41**, 547–559.
26 P. Maitre, D. Scuderi, D. Corinti, B. Chiavarino, M. E. Crestoni and S. Fornarini, *Chem. Rev.*, 2020, **120**, 3261–3295.
27 B. Chiavarino, L. Rotari, M. E. Crestoni, D. Corinti, D. Scuderi and J.-Y. Salpin, *Inorg. Chem.*, 2025, **64**, 4873–4883.
28 D. Corinti, G. Berden, J. Oomens, B. Martinez-Hay, S. Fornarini and M. E. Crestoni, *Int. J. Mass Spectrom.*, 2024, **505**, 117322.
29 D. Corinti, A. De Petris, C. Coletti, N. Re, B. Chiavarino, M. E. Crestoni and S. Fornarini, *ChemPhysChem*, 2017, **18**, 318–325.
30 D. Corinti, B. Chiavarino, M. Spano, A. Tintaru, S. Fornarini and M. E. Crestoni, *Anal. Chem.*, 2021, **93**, 14869–14877.
31 D. Oepts, A. F. G. van der Meer and P. W. van Amersfoort, *Infrared Phys. Technol.*, 1995, **36**, 297–308.
32 J. Martens, G. Berden, C. Gebhardt and J. Oomens, *Rev. Sci. Instrum.*, 2016, **87**, 103108.
33 G. Berden, M. Derksen, K. J. Houthuijs, J. Martens and J. Oomens, *Int. J. Mass Spectrom.*, 2019, **443**, 1–8.
34 J. S. Prell, J. T. O'Brien and E. R. Williams, *J. Am. Soc. Mass Spectrom.*, 2010, **21**, 800–809.
35 F. A. M. G. van Geenen, R. F. Kranenburg, A. C. van Asten, J. Martens, J. Oomens and G. Berden, *Anal. Chem.*, 2021, **93**, 2687–2693.
36 E. P. Ávila, L. A. O. Mendes, W. B. de Almeida, H. F. dos Santos and M. V. de Almeida, *J. Mol. Struct.*, 2021, **1245**, 131027.
37 R. Sekine, E. G. Robertson and D. McNaughton, *Vib. Spectrosc.*, 2011, **57**, 306–314.
38 D. Corinti, A. Maccelli, B. Chiavarino, P. Maitre, D. Scuderi, E. Bodo, S. Fornarini and M. E. Crestoni, *J. Chem. Phys.*, 2019, **150**, 165101.
39 M. J. Frisch, G. W. Trucks, H. B. Schlegel, G. E. Scuseria, M. A. Robb, J. R. Cheeseman, G. Scalmani, V. Barone, G. A. Petersson, H. Nakatsuji, X. Li, M. Caricato, A. V. Marenich, J. Bloino, B. G. Janesko, R. Gomperts, B. Mennucci, H. P. Hratchian, J. V. Ortiz, A. F. Izmaylov, J. L. Sonnenberg, D. Williams-Young, F. Ding, F. Lipparini, F. Egidi, J. Goings, B. Peng, A. Petrone, T. Henderson, D. Ranasinghe, V. G. Zakrzewski, J. Gao, N. Rega, G. Zheng, W. Liang, M. Hada, M. Ehara, K. Toyota, R. Fukuda, J. Hasegawa, M. Ishida, T. Nakajima, Y. Honda, O. Kitao, H. Nakai, T. Vreven, K. Throssell, J. A. Montgomery Jr., J. E. Peralta, F. Ogliaro, M. J. Bearpark, J. J. Heyd, E. N. Brothers, K. N. Kudin, V. N. Staroverov, T. A. Keith, R. Kobayashi, J. Normand, K. Raghavachari, A. P. Rendell, J. C. Burant, S. S. Iyengar, J. Tomasi, M. Cossi, J. M. Millam, M. Klene, C. Adamo, R. Cammi, J. W. Ochterski, R. L. Martin, K. Morokuma, O. Farkas, J. B. Foresman and D. J. Fox, *Gaussian 16, Revision C.01*, Gaussian, Inc., Wallingford, CT, 2016.
40 M. Biczysko, P. Panek, G. Scalmani, J. Bloino and V. Barone, *J. Chem. Theory Comput.*, 2010, **6**, 2115–2125.
41 R. Boussessi, G. Ceselin, N. Tasinato and V. Barone, *J. Mol. Struct.*, 2020, **1208**, 127886.
42 D. Corinti, M. E. Crestoni, B. Chiavarino, S. Fornarini, D. Scuderi and J.-Y. Salpin, *J. Am. Soc. Mass Spectrom.*, 2020, **31**, 946–960.
43 F. Cuyckens and M. Claeys, *J. Mass Spectrom.*, 2004, **39**, 1–15.
44 R. Marcha and J. Brodbelt, *J. Mass Spectrom.*, 2008, **43**, 1581–1617.
45 N. C. Polfer and J. Oomens, *Mass Spectrom. Rev.*, 2009, **28**, 468–494.
46 E. P. Ávila, L. A. O. Mendes, W. B. de Almeida, H. F. dos Santos and M. V. de Almeida, *J. Mol. Struct.*, 2021, **1245**, 131027.
47 C. Jiang and P. J. Gates, *Molecules*, 2024, **29**, 5246.
48 P. J. A. Madeira, C. M. Borges and M. H. Florêncio, *Rapid Commun. Mass Spectrom.*, 2010, **24**, 3432–3440.
49 H. Song and H. Guo, *ACS Phys. Chem. Au*, 2023, **3**, 406–418.

